Front. Struct. Civ. Eng. 2021, 15(2): 333–345
https://doi.org/10.1007/s11709-021-0718-8

RESEARCH ARTICLE

Experimental study on slurry-induced fracturing during shield tunneling

Teng WANG, Dajun YUAN, Dalong JIN*, Xinggao LI

Key Laboratory of Urban Underground Engineering of the Education Ministry, Beijing Jiaotong University, Beijing 100044, China
**Corresponding author. E-mail: jindalong@163.com*

ABSTRACT Facial support in slurry shield tunneling is provided by slurry pressure to balance the external earth and water pressure. Hydraulic fracturing may occur and cause a significant decrease in the support pressure if the slurry pressure exceeds the threshold of the soil or rock material, resulting in a serious face collapse accident. Preventing the occurrence of hydraulic fracturing in a slurry shield requires investigating the effects of related influencing factors on the hydraulic fracturing pressure and fracture pattern. In this study, a hydraulic fracturing apparatus was developed to test the slurry-induced fracturing of cohesive soil. The effects of different sample parameters and loading conditions, including types of holes, unconfined compressive strength, slurry viscosity, and axial and circumferential loads, on the fracturing pressure and fracture dip were examined. The results indicate that the fracture dip is mainly affected by the deviator stress. The fracturing pressure increases linearly with the increase in the circumferential pressure, but it is almost independent of the axial pressure. The unconfined compressive strength of soil can reflect its ability to resist fracturing failure. The fracturing pressure increases with an increase in the unconfined compressive strength as well as the slurry viscosity. Based on the test results, an empirical approach was proposed to estimate the fracturing pressure of the soil.

KEYWORDS slurry shield tunneling, hydraulic fracturing test, fracturing pressure, fracture dip, unconfined compressive strength, slurry viscosity

1 Introduction

Slurry shield tunnel boring machines are widely used for tunneling in soft ground with shallow soil cover and under seas or rivers. The face support of the slurry shield tunnel boring machine is provided by slurry counterpressure, namely, a suspension of bentonite or a clay and water mixture (slurry). When tunneling using a slurry shield tunnel boring machine, the tunnel face stability is significantly influenced by filter cake formation during slurry injection into the chamber [1]. To form the filter cake and maintain face stability, the slurry pressure is usually greater than the external soil and water pressure, as illustrated in Fig. 1(a). However, hydraulic fracturing may occur and cause a significant decrease in the support pressure if the slurry pressure exceeds the threshold of the soil or rock material, resulting in a serious face collapse accident [2–4]. A schematic of the hydraulic fracturing caused by excess slurry pressure is shown in Fig. 1(b). Therefore, it is necessary to study slurry-induced fracturing during shield tunneling.

During the past decades, hydraulic fracturing has been widely used in oil and gas exploitation and has attracted extensive attention worldwide [5–7]. Lockner and Byerlee [8] pointed out that the failure mode of hydraulic fracturing is related to the high confining pressure and differential stresses. The hydraulic fracturing pressure is influenced by the pressurizing rate and viscosity of the liquid in the borehole [9–11]. Hydraulic fracturing in soil is also used in chemical grouting [12–15]. Bjerrum et al. [16] studied the behavior of hydraulic fracturing in soil and proposed applying hydraulic fracturing in estimating soil permeability. In the case of backfill grouting and anchor injection in the construction of tunnels, fracturing by excess injection pressure has also been observed [17]. Additionally, unexpected hydraulic fracturing may cause serious accidents, such as collapse in dam engineering [18,19]. Vaughan [20] and Jaworski et al. [21] performed fracture

Article history: Received Apr 13, 2020; Accepted Sep 22, 2020

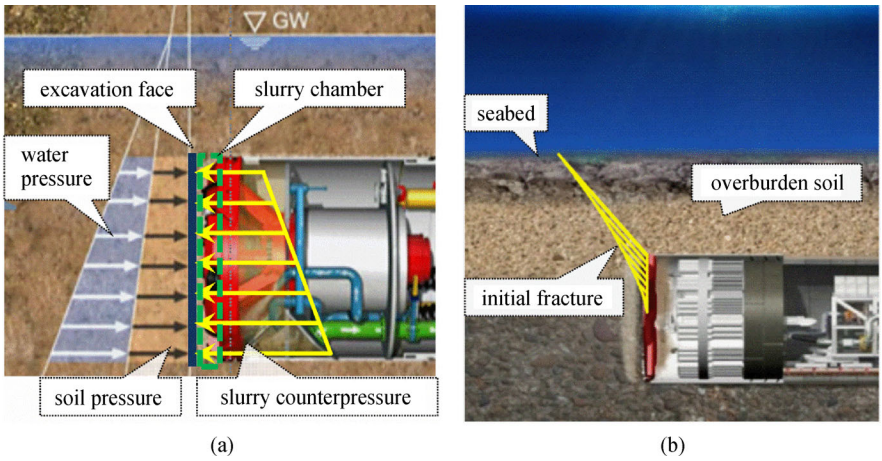

Fig. 1 Drawings showing hydraulic fracturing in shield tunneling. (a) Stress state of excavation face; (b) shape of the initial fracture.

tests on compacted soils to investigate the failure of Teton Dam and found that the hydrofracturing pressure was related to the horizontal stress and apparent tensile strength. Mori and Tamura [22] and Mori et al. [23] investigated the relationship between the hydraulic fracturing pressure and soil strength and found that the fracturing pressure was related to the minimum principal stress and the unconfined compressive strength of soil. Furthermore, with the rapid increase in computing power, numerical tools have become an attractive option for investigating the fracturing process in the past few years. Zhuang et al. [24] and Zhou et al. [25–27] introduced a phase-field modeling approach for fracture propagation in poroelastic media. The phase-field method for dynamic cracks in a single-phase solid was extended for fluid-driven dynamic cracks and agrees well with existing analytical methods. Other new approaches for modeling and simulation of the fracturing process have also been introduced [28–30]. These methods can handle crack branching and fragmentation effectively and reproduce the fracturing process clearly, playing an important role in the study of crack extension in soils.

However, most of the research focuses on the fracture induced by water pressure, and knowledge of slurry-induced fracture during shield tunneling remains limited. According to existing research [31,32], viscosity reduces seepage and increases the flow resistance of the liquid in cracks, which may cause the fracturing induced by water and slurry to be very different. Therefore, previous studies cannot be directly used in shield tunnel engineering. Moreover, hydraulic fracturing tests were performed using a series of through-hole cylinder samples, whose failure mode may be different from that of the tunnel face. In this study, a hydraulic fracturing apparatus was developed to test the slurry-induced fracturing of cohesive soil. To simulate the failure mode of shield tunnels, two types of samples with blind holes and through holes were prepared for the tests. The effects of different factors, including sample types, unconfined compressive strength of soil, slurry viscosity, and loading conditions, on the fracturing pressure and fracture dip were examined. Based on the test results, an empirical approach was proposed to estimate the fracturing pressure of the soil, providing references for setting the slurry counterpressure during slurry shield tunneling.

2 Hydraulic fracturing experiment

2.1 Apparatus

In this study, an apparatus was developed for hydraulic fracturing tests of cohesive soil. As shown in Fig. 2, the apparatus consists of four parts: a loading system, a programmable logic controller (PLC) control system, a monitoring system, and a test chamber. The test chamber was a hollow cylinder with a height of 16 cm and a diameter of 13 cm, as shown in Fig. 3(a). A rubber sleeve was placed in the chamber to seal the soil samples. The circumferential pressure acting on the soil sample was provided by oil in the test chamber, and the pressure could be adjusted by using a hydraulic pump. There are caps on the ends of the test chamber, and a hydraulic jack was applied on the top of the soil sample to provide the axial load. Slurry pressure was applied to the inside of the soil sample through a hole at the bottom. Three sensors (a load cell and two pressure gauges) were used to monitor the corresponding load. The precisions of the load cell and pressure gauges were 1.0 g and 1.0 kPa, respectively. All the sensors were connected to the PLC control system shown in Fig. 3(b) to collect and record data in real time.

The sample prepared in advance was wrapped in a rubber sleeve and placed into the test chamber. The sample base connected to the grouting pipe was placed at the bottom cover, and then the top cover was installed in the test chamber. The axial load and circumferential pressure

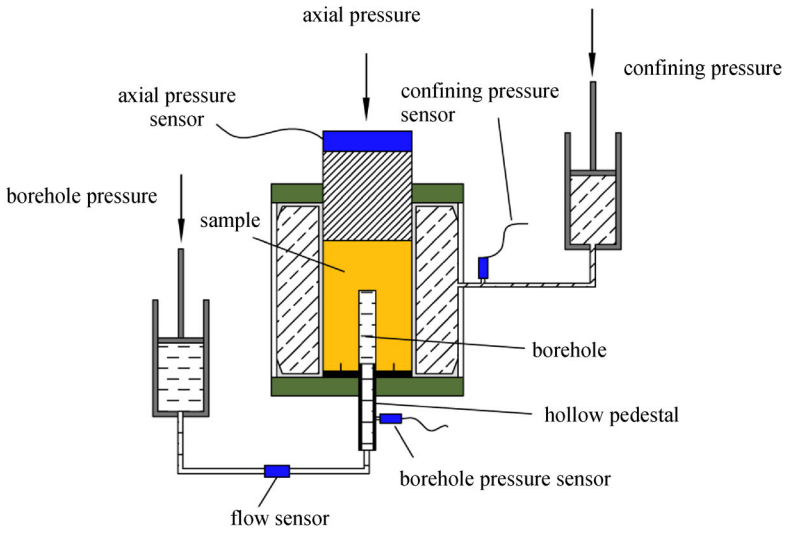

Fig. 2 Schematic of the fracturing test equipment.

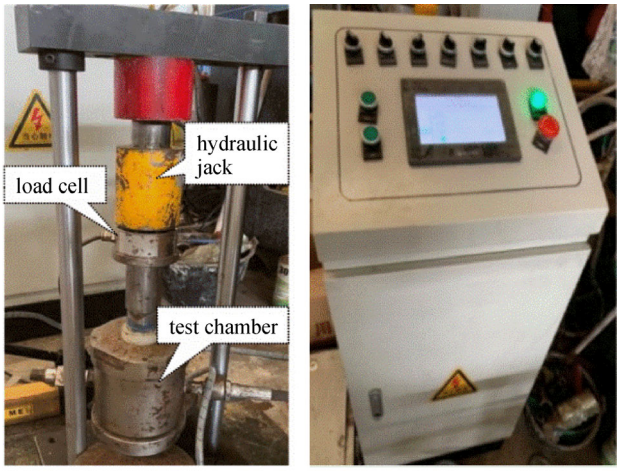

Fig. 3 Photographs showing details of the slurry fracturing test apparatus. (a) Test chamber; (b) PLC control system.

were set to specified values, and then the slurry injection pressure was increased continuously until the sample fractured. Finally, all three pressures were unloaded simultaneously to prevent the samples from being damaged by uneven unloading. After unloading, the sample was removed for observation and recording.

2.2 Material

Because it is difficult to guarantee the homogeneity of samples using disturbed soil and the fracturing process may be greatly affected by random defects in samples, artificial clay with a homogeneous structure was adopted in preparing samples in this study. This enabled the mechanical parameters of samples to be adjusted for more extensive parametric studies by changing the material ratios. Based on previous studies, the fracturing pressure depends significantly on the unconfined compressive strength. Therefore, the unconfined compressive strength of artificial clay with different material ratios was tested. The composition of artificial clay includes aggregates and cementation. In this study, kaolin clay and bentonite were selected as the aggregate, and gypsum was selected as the cementing material. To ensure the homogeneity of the samples, soil pastes were obtained by mixing three materials with water, pouring the mixtures into molds, and allowing them to solidify to form samples. The good fluidity of the soil paste ensured the compactness and homogeneity of the poured sample. Samples with different strengths were obtained, and the corresponding material ratios of kaolin, gypsum, bentonite, and water are listed in Table 1.

To study the effect of slurry viscosity on fracturing pressure, slurries with different viscosities were also prepared to perform fracturing tests. The components of the slurry were water, bentonite, and carboxymethyl cellulose. As shown in Fig. 4, the slurry was dyed red to observe the fracture shape clearly, and the slurry viscosity was measured using a 700 mL funnel viscosimeter. The viscosities of the slurries with different material ratios are listed in Table 2.

2.3 Samples and loading conditions

As shown in Figs. 5(a) and 5(b), the mold for the sample preparation was cylindrical with a central axis. The height and outer diameter of the mold were 100 and 100 cm, respectively. The mold was equipped with two different bases to prepare samples with through holes and blind holes, and the heights of the central axis of the bases were 100 and 50 cm, respectively. The samples were prepared in molds using a casting method [22,23]. The molds were placed on a small shaking table to eliminate air bubbles in the soil paste during pouring. Vaseline was smeared on the

Table 1 Material ratios of different unconfined compressive strengths

kaolin (g)	gypsum (g)	bentonite (g)	water (g)	unconfined compressive strength (MPa)
778	500	389	1000	0.100
742	573	353	1000	0.167
703	647	315	1000	0.239
667	721	279	1000	0.364
629	796	240	1000	0.413
593	870	204	1000	0.692
557	942	169	1000	0.713

Fig. 4 Photograph showing measurement of slurry viscosity.

Table 2 Material ratios of slurry with different viscosities

water (g)	bentonite (g)	carboxymethyl cellulose (g)	viscosity (s)
1000	0	0	15
935	65	0	18
899	101	5	21
853	147	10	24
814	186	12	27
746	254	14	28.5
746	254	17	30
746	254	21	33

inner side of the molds to facilitate demolding. Then, the samples were placed for a period of time until they solidified, after which the samples were demolded. Additionally, the same batch of soil material was used for the unconfined compressive tests. Figure 5(c) shows a solidified sample with good homogeneity; the homogeneity minimizes interference from random defects on the test results.

In this study, the effects of different sample parameters and loading conditions, including types of holes, unconfined compressive strength, slurry viscosity, and axial and circumferential loads, on the fracturing pressure and fracture dip were examined. The radius and height of the samples in all cases were 25 and 100 mm, respectively. Owing to the stress concentration on the tunnel face, two different types of injection holes, namely, through and blind holes, as shown in Figs. 6(a) and 6(b), were set in these samples. The unconfined compressive strength of the soil material ranged from 0.1 to 0.71 MPa. The slurry viscosity ranged from 15 to 33 s. The details of the sample parameters and loading conditions are presented in Table 3.

3 Characteristics of fracturing pressure and fracture dip

3.1 Fracturing pressure

Figure 7 presents the development of the slurry pressure in the center hole during the test process. The changes in the circumferential and axial loads are plotted in this figure. Sample C with a blind hole was used in this test, and the slurry viscosity was 33 s. The axial and circumferential loads were 0.4 and 0.5 MPa, respectively. As shown in Fig. 7, the loading process during the fracturing test can be conducted in four stages: (a) initial loading, (b) loading stabilization, (c) increase in the slurry loading, and (d) fracturing failure. During the initial loading, all the loads, including the axial load, circumferential load, and slurry load, increase to the specified values in the first 40 s. During loading stabilization, all the loads are kept stable for 10 s. During the increase in the slurry loading, after 50 s, the slurry pressure in the center hole starts to increase again, while the circumferential and axial loads remain constant. During this stage, there are no through cracks in the soil sample, and fracturing failure does not occur. The slurry pressure reaches a peak at 67 s and the corresponding value is 1.32 MPa. Finally, during fracturing failure, through cracks occur in the soil sample and the slurry pressure as well as the axial and circumferential loads rapidly decrease to zero. The peak value of the slurry pressure before fracturing failure can be considered as the fracturing pressure.

3.2 Fracture dip

Because the pressurized liquid was dyed red in advance, the fracture surface in the soil samples could be clearly observed. Figure 8(a) shows a fractured soil sample with a blind hole after the fracturing test in which the axial and circumferential loads are 0.4 MPa. It can be seen that the fracture extends obliquely from the bottom of the center hole to the surface at an angle, which is called the fracture dip. The fracture pattern of samples with blind holes is

(a) (b) (c)

Fig. 5 Mold and sample: (a) mold; (b) mold base; (c) solidified sample.

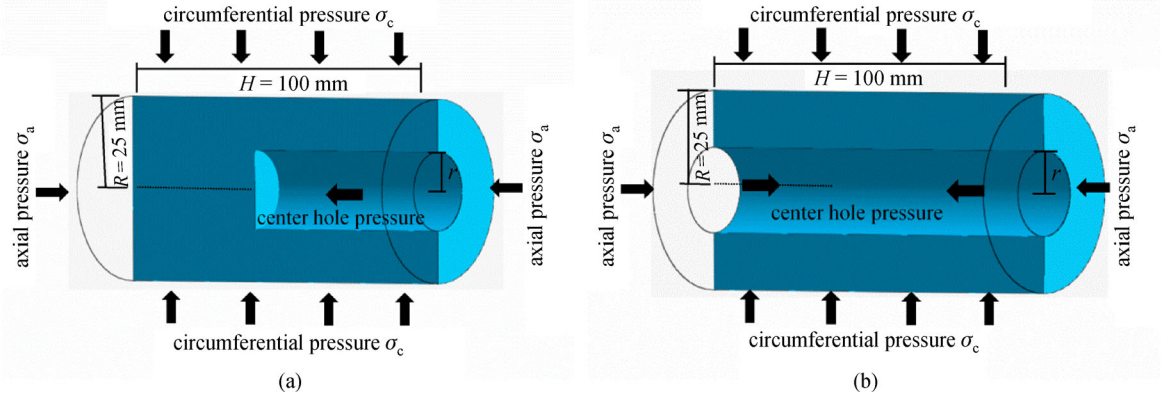

Fig. 6 Center hole type: (a) through; (b) blind.

Table 3 Sample parameters and loading conditions

sample	H (mm)	R (mm)	r (mm)	σ_c (MPa)	σ_a (MPa)	q_u (MPa)	v (s)	center hole type
A1	100	25	9	0.3, 0.4, 0.5, 0.6, 0.7	0.4 0.5	0.71	18	blind/through
A2	100	25	9	0.4 0.5 0.6	0.3, 0.4, 0.5, 0.6, 0.7	0.71	18	blind/through
B	100	25	9	0.2	0.2	0.1, 0.17, 0.24, 0.36, 0.41, 0.69, 0.71	18	blind/through
C	100	25	9	0.5	0.4, 0.5	0.71	15, 18, 21, 24, 27, 28.5, 30, 33	blind

Notes: H = sample height; R = sample radius; r = center hole radius; σ_c = circumferential pressure; σ_a = axial pressure; q_u = unconfined compressive strength; v = slurry viscosity.

similar to that in tunnels described by Yuan [2], as shown in Fig. 9. The fracture dip of this sample was ~45°. Figure 8(b) shows a fractured soil sample with a through hole. In contrast to samples with blind holes, the fracture of samples with through holes follows the generatrix. The samples are usually broken into two parts, and the fracture shapes under different loading conditions are nearly the same.

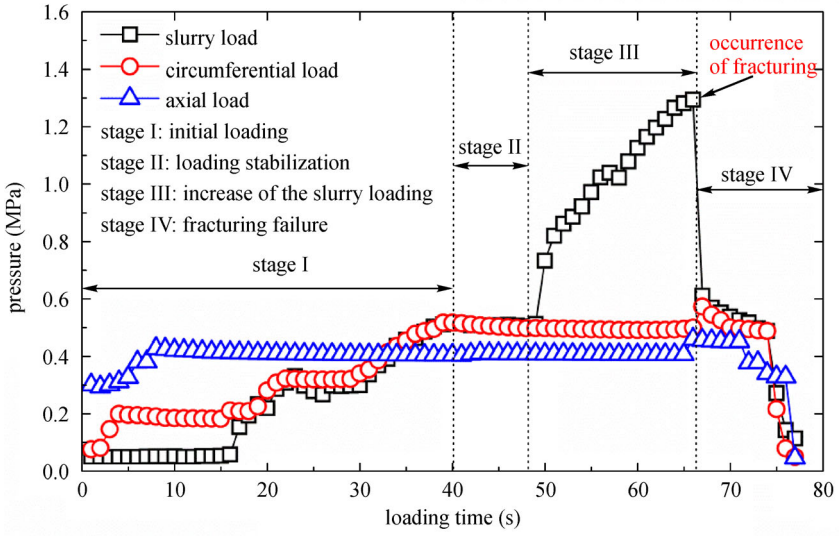

Fig. 7 Loading change during fracturing test on sample C with a blind hole.

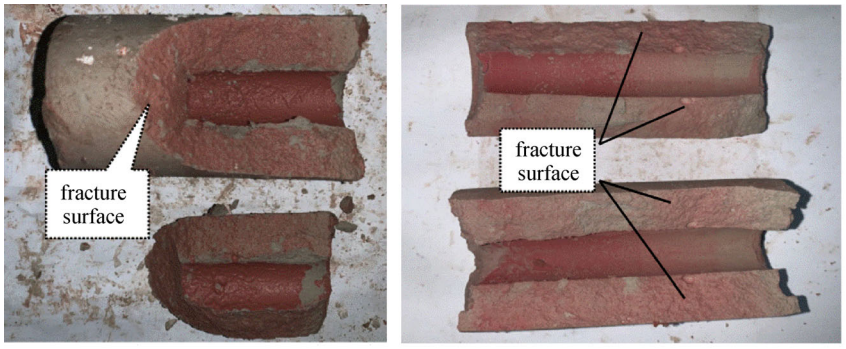

Fig. 8 Fracture surface of two kinds of samples: (a) the sample with blind hole; (b) the sample with through hole.

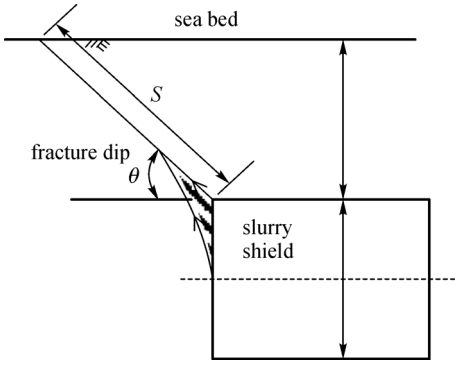

Fig. 9 Diagram of the fracture shape in tunnels.

4 Parametric analyses

4.1 Loading conditions

The circumferential and axial pressures acting on the soil sample are important factors in the occurrence of fracturing. To study the influence of the circumferential pressure on the fracturing pressure and fracture dip, fracturing tests were conducted on sample A1 under different circumferential pressures varying from 0.3 to 0.7 MPa. Two levels of axial pressure were set, i.e., 0.4 and 0.5 MPa. The unconfined compressive strength was 0.71 MPa. A slurry with a viscosity of 18 s was used in the tests to apply the center hole load. Figure 10 shows the variation in the fracturing pressure at different circumferential pressures. A linear relationship was found between the fracturing and circumferential pressures. This is because circumferential pressure can resist fracturing. The greater the circumferential pressure, the higher is the fracturing pressure. Consequently, a higher overburden of the tunnel can help resist fracturing induced by shield tunneling. With the increase in circumferential pressure, the fracturing pressure of samples with a blind hole is slightly greater than that with a through hole. This is because the samples with through holes mainly undergo tensile failure, whereas the samples with blind holes undergo the combined effects of tensile and shear failures.

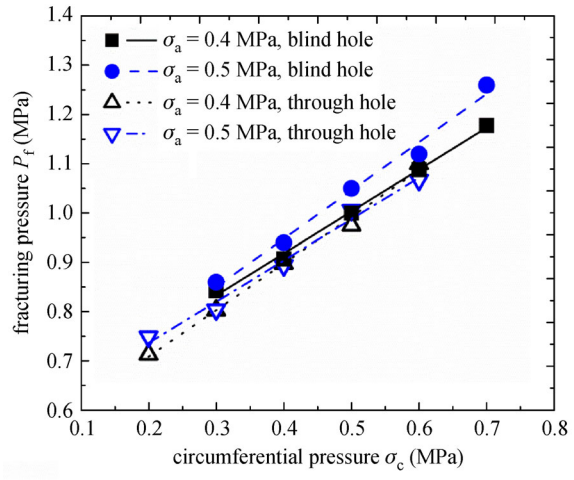

Fig. 10 Variation of fracturing pressure with circumferential pressure.

To investigate the influence of the axial pressure on the fracturing pressure and fracture dip, fracturing tests were conducted on sample A2 under different axial pressures ranging from 0.3 to 0.7 MPa. Three levels of circumferential pressure with values of 0.4, 0.5, and 0.6 MPa were set. The unconfined compressive strength was 0.71 MPa, and a slurry with a viscosity of 18 s was adopted. Figure 11 shows the variation in the fracturing pressure at different axial pressures. It can be seen that the fracturing pressure varies slightly with the axial pressure under the three levels of circumferential pressure. Additionally, the fracturing pressures of samples with blind holes were again found to be slightly larger than those with through holes.

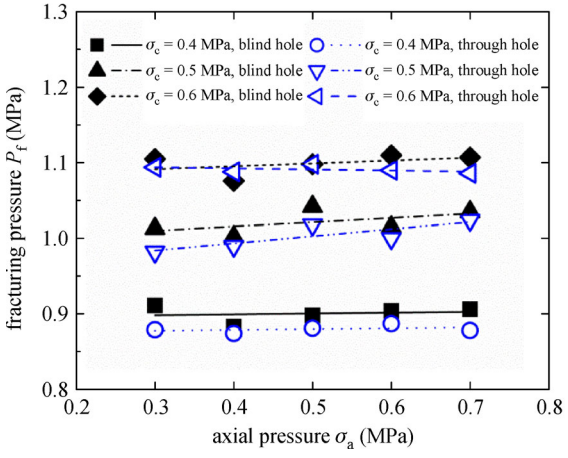

Fig. 11 Variation of fracturing pressure with axial pressure.

From the test results, it is observed that the fracture dips of the blind-hole samples change with circumferential and axial pressures, while the fracture shapes of all through-hole samples are nearly the same. Only the fracture dips of the samples with blind holes were investigated in this study. Figure 12(a) shows the variation in the fracture dip of blind-hole samples with circumferential pressure under the same axial pressure. It can be seen that the fracture dip increases linearly with the increase in circumferential pressure; that is, the larger the circumferential pressure, the more the fracture extends toward the circumferential direction. When the circumferential pressure is kept constant, the variation in the fracture dip of the blind-hole samples with axial pressure is shown in Fig. 12(b). It is found that the fracture dip decreases with the increase in axial pressure, which indicates that the fracture tends to be parallel to the axial direction under higher axial pressure conditions. By incorporating the effects of both the circumferential and axial pressures shown in Figs. 12(a) and 12(b), it can be concluded that the fracture in tunnels is prone to extend toward the direction of higher pressure. This is because the fracture occurs in the direction perpendicular to the minimum principal stress and extends along the maximum principal stress [33,34].

Based on elastic–plastic mechanics, the volume change of the material depends on the principal stress, while the deformation depends on the state of the deviator stress when it enters the plastic state. The influence of the deviator stress on the fracture dip is investigated by considering that plastic failure occurs when soil samples are fractured. Deviator stress $\sigma_a - \sigma_c$ is defined as the difference between the axial pressure σ_a and circumferential pressure σ_c in the triaxial test done by Xu [35], which was also adopted in the fracturing tests in this study. Figure 13 shows the variation in the fracture dip of the blind-hole samples with deviator stress $\sigma_a - \sigma_c$. From the figure, it can be seen that the fracture dip decreases linearly with an increase in deviator stress. Although the axial and circumferential pressures are different, the fracture dip is basically the same as long as the deviator stress $\sigma_a - \sigma_c$ is the same, which means that the fracture dip mainly depends on the deviator stress. The fracture dip was ~45° for zero deviator stress. When the deviator stress $\sigma_a - \sigma_c$ was < -0.3 MPa, the fracture dip increased to 90°; that is, the fracture was perpendicular to the sample axis, as shown in Fig. 14.

To verify the accuracy of the variation of the fracture dip of blind-hole samples with deviator stress, more fracturing tests were conducted under deviator stresses of 0.1 and -0.1 MPa. The circumferential and axial pressures were variable at each level of deviator stress. Figure 15 shows the variation of the fracture dip of blind-hole samples with circumferential pressure when the deviator stress is 0.1 and -0.1 MPa. It can be clearly seen that, when the deviator stress is constant, the fracture dip does not change with circumferential pressure. The fracture dips at different circumferential pressures are ~30° for a deviator stress of 0.1 MPa. When the deviator stress is -0.1 MPa, the fracture dips are ~50°, which are in accordance with the results shown in Fig. 13. Two examples of fractured samples with blind holes under these two levels of deviator

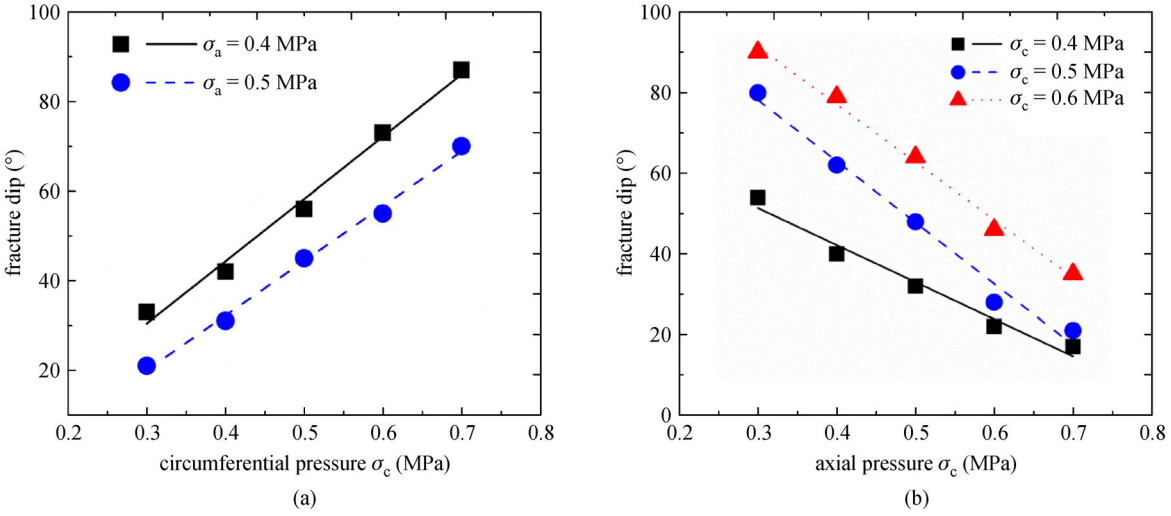

Fig. 12 Variation of fracture dip of blind-hole samples with (a) circumferential and (b) axial pressure.

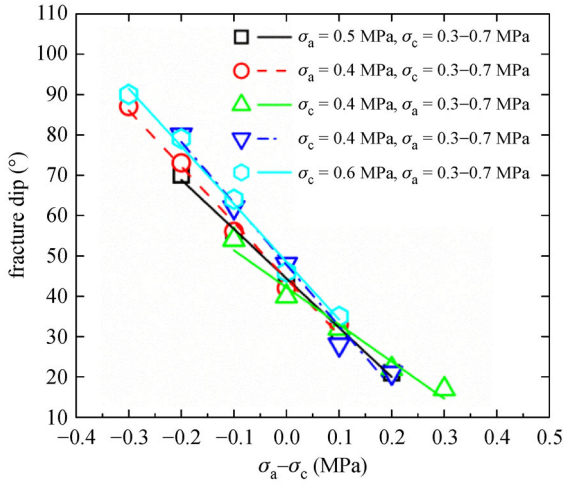

Fig. 13 Variation of fracture dip of blind-hole samples with $\sigma_a - \sigma_c$.

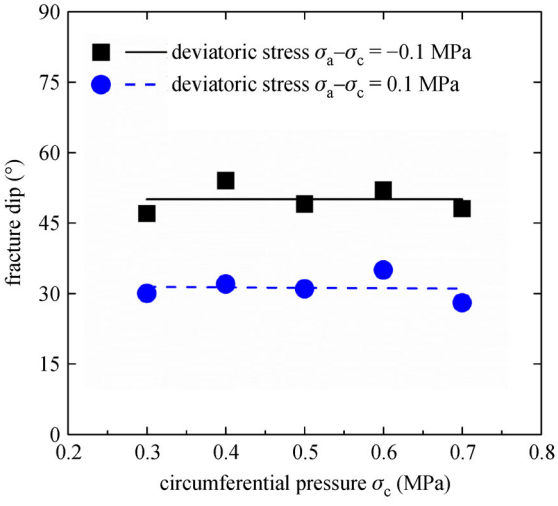

Fig. 15 Variation of fracture dip with circumferential pressure under constant deviator stress.

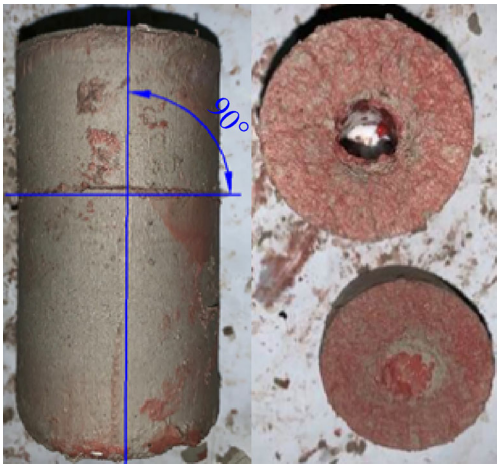

Fig. 14 Photograph showing fracture perpendicular to the sample axis.

stress are shown in Fig. 16. The results further verify that the fracture dip of a sample with a blind hole is mainly related to the deviator stress.

4.2 Unconfined compressive strength

The unconfined compressive strength is widely acknowledged as a vital factor for hydraulic fracturing of soil. In this parametric study, seven different unconfined compressive strengths ranging from 0.1 to 0.71 MPa were considered. Figure 17 shows the effect of the unconfined compressive strength on the fracturing pressure of the soil. Both the axial and circumferential pressures acting on the soil sample were 0.2 MPa. The viscosity of the slurry used in this test was 18 s. It can be clearly seen from Fig. 17 that the fracturing pressure of the soil exhibits a linear increasing tendency with an increase in the unconfined

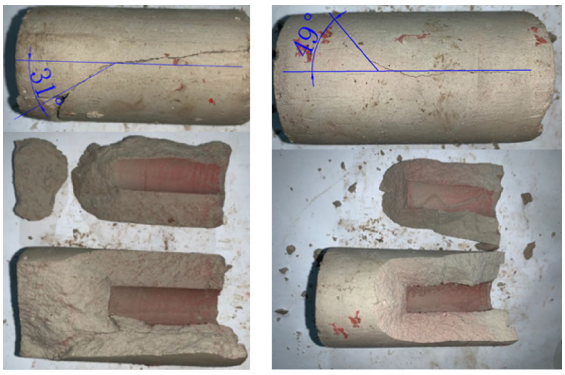

Fig. 16 Photographs of fracture dip and fracture surface of samples with blind holes under constant deviator stress: (a) – 0.1 MPa deviator stress; (b) 0.1 MPa deviator stress.

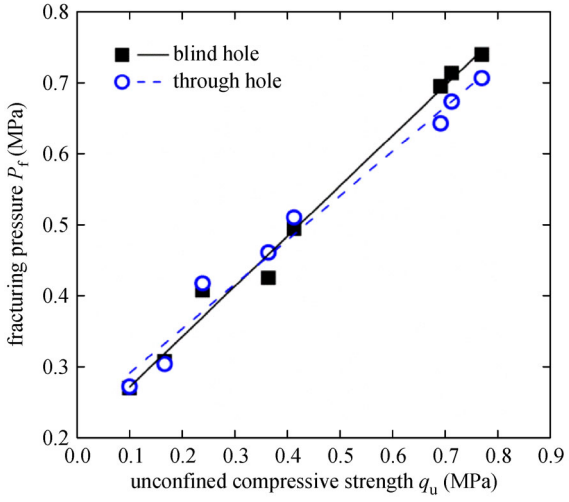

Fig. 17 Variation of fracturing pressure with unconfined compressive strength.

compressive strength. This can be understood by the fact that a higher unconfined compressive strength can enhance the capacity to resist fracturing failure.

4.3 Slurry viscosity

During tunneling using a slurry shield machine, the slurry viscosity is usually adjusted based on the encountered soil properties and slagging capacity. To study the effect of slurry viscosity on soil fracturing, a series of tests were performed using slurries with different viscosities varying from 15 to 33 s. The designed mix ratios of the adopted slurries are listed in Table 2. The circumferential pressure was 0.5 MPa and two axial pressures with values of 0.4 and 0.5 MPa were set in the experiments. The unconfined compressive strength of the sample was 0.71 MPa. Because the type of samples has only a minor impact on the fracturing pressure, samples with blind holes were selected for the test in this section. Figure 18 shows the effect of slurry viscosity on the soil fracturing pressure. It can be seen that the fracturing pressure increases with an increase in slurry viscosity. However, when the slurry viscosity was >27 s, the fracturing pressure almost stabilized at 1.3 MPa and barely increased any further. This is because micro-fractures usually occur before fracturing failure, and the micro-fractures are easily penetrated by the low-viscosity slurry, which in turn contributes to the development of additional micro-fractures. The effect of slurry viscosity on the fracture dip is shown in Fig. 19. The fracture dip fluctuates slightly within a narrow range with the increase in slurry viscosity in the two cases, indicating that it is slightly affected by the slurry viscosity. This is because the fracture dip depends on the direction of the principal stress, whereas the change in slurry viscosity does not affect the direction of the principal stress. In the case in which $\sigma_a = 0.4$ MPa and

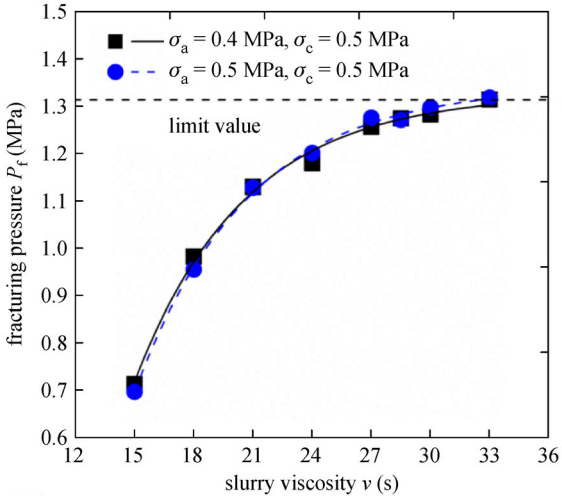

Fig. 18 Variation of fracturing pressure with slurry viscosity.

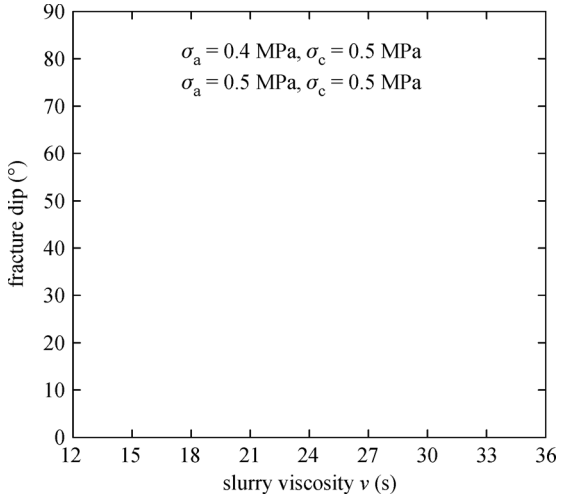

Fig. 19 Variation of fracture dip with slurry viscosity.

$\sigma_c = 0.5$ MPa, the fracture dip varies in the range of 49°–53°. The fracture dip is 41°–47° for the cases in which $\sigma_a = 0.5$ MPa and $\sigma_c = 0.5$ MPa. The results of these two cases agree with the results shown in Fig. 13.

5 Discussion

Mori and Tamura [22] and Mori et al. [23] investigated the relationship between the hydraulic fracturing pressure and confining stress by conducting laboratory tests on cylindrical samples with through boreholes. They suggested the following equation for estimating the fracturing pressure:

$$P_f = \sigma_3 + \alpha q_u, \tag{1}$$

where σ_3 is the confining stress, q_u is the unconfined compressive strength, and α is the coefficient related to the viscosity of the pressurized liquid.

To quantitatively estimate the fracturing pressure at the excavation face in tunnels, a fitting process was conducted on the test results of samples with a blind hole. As shown in Fig. 20, the relationship between the fracturing pressure and circumferential pressure in the above tests can be linearly fitted with an R^2 value of 0.96. It can be seen that the slope of the linear function is almost 1.0, which follows Eq. (1) for the through-hole cases proposed by Mori and Tamura [22] and Mori et al. [23]. Intercepts of all fitted lines are basically the same. This is because the unconfined compressive strength of the samples and the slurry viscosity in the four cases are the same. To study the relationship between the fracturing pressure P_f and unconfined compressive strength q_u, the relationship between $P_f - \sigma_c$ and q_u was analyzed and fitted, as shown in Fig. 21. It can be concluded that the equation for the fracturing pressure of samples with blind holes is $P_f = \sigma_c + 0.7q_u$, satisfying Eq. (1) for the through-hole cases. The R^2 value in this regression is 0.99, indicating that the equation fits well with the test data.

To determine the relationship between the fracturing pressure and slurry viscosity, the variation of the coefficient α with slurry viscosity is plotted in Fig. 22. An exponential curve was used to fit the test data. The fitted fracturing pressure of the soil can be expressed as

$$P_f = \sigma_c + \left(-14e^{-\frac{v}{5.4}} + 1.2\right)q_u, \tag{2}$$

where σ_c is the circumferential stress, q_u is the unconfined compressive strength, and v is the slurry viscosity; R^2 is 0.99.

Figure 23 shows the comparison between the test results and the prediction of the fracturing pressure using Eq. (2). An error range of ±5% is also shown in the figure. It can be

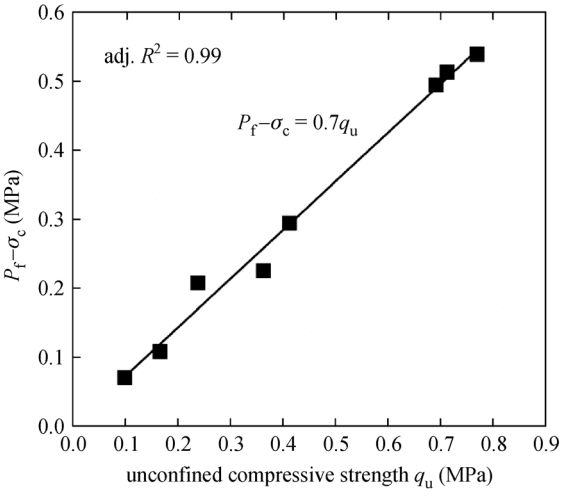

Fig. 21 Relationship between $P_f - \sigma_c$ and unconfined compressive strength of samples with a blind hole.

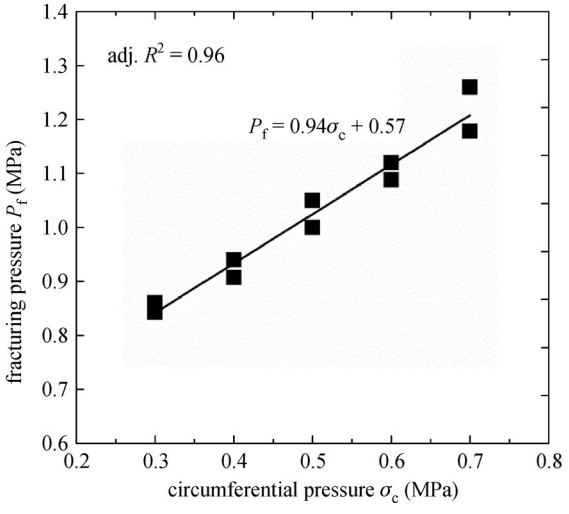

Fig. 20 Relationship between fracturing pressure and circumferential pressure of samples with a blind hole.

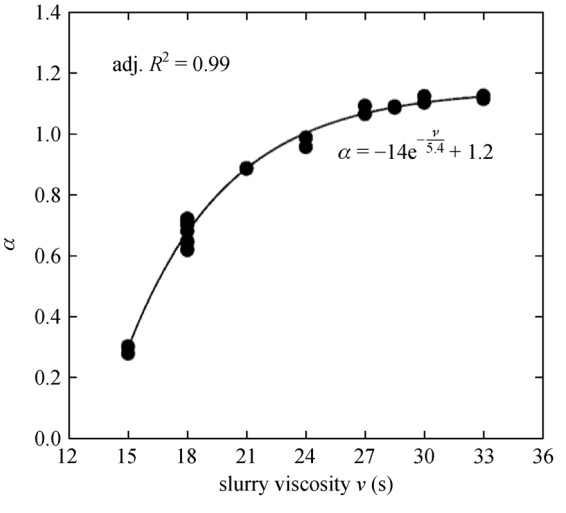

Fig. 22 Relationship between the coefficient α and slurry viscosity of samples with a blind hole.

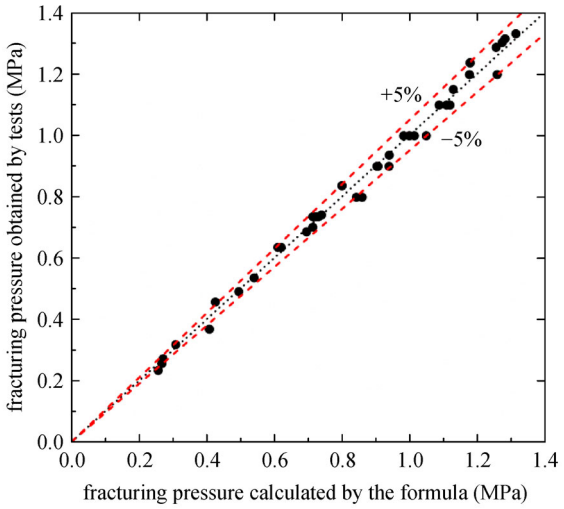

Fig. 23 Comparison of the test results and prediction of fracturing pressure.

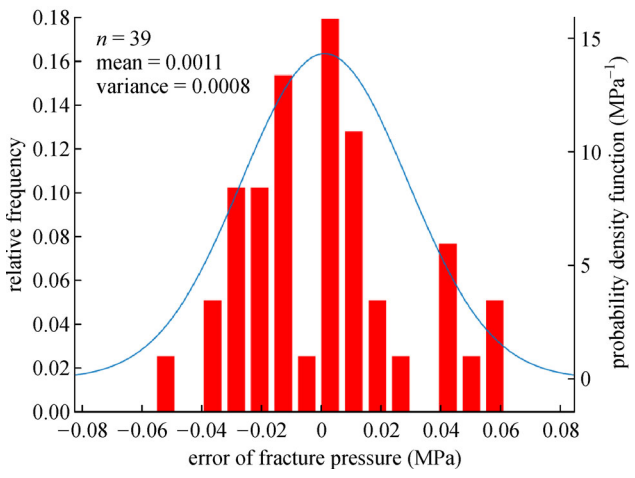

Fig. 24 Distribution of errors between test data and predicted results.

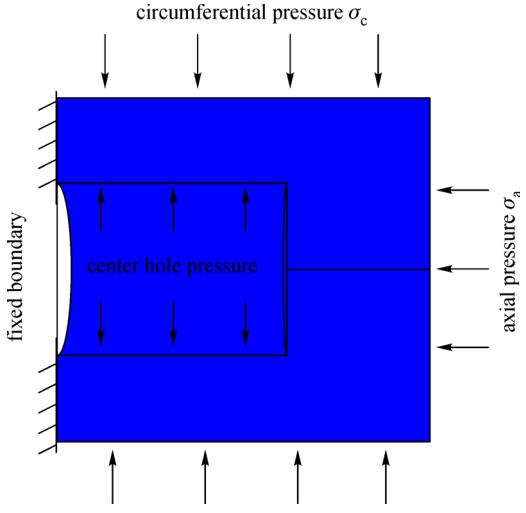

Fig. 25 Boundary and loading conditions of the model in the numerical simulation.

seen that almost all the fracturing pressures were within the ±5% range. To further test the goodness of fit in the regression analysis of fracture pressure, a statistical analysis was conducted to present the probability density function [36–38]. Figure 24 shows the statistical results of the errors between the test data and the predicted values. The fracture pressure error can be described by a normal distribution in which the variance and mean values are 0.001 and 0.0008, respectively. It can be seen that the mean value of the errors is small enough and the statistical dispersion of the distribution is very slight, indicating good applicability of the proposed approach.

Additionally, numerical simulation is an effective method employed in hydraulic fracturing research [24–30]. To verify the relationship between the fracture dip and loading conditions, the extended finite element method (XFEM) was used to simulate the hydraulic fracturing of a sample with a blind hole under various loading conditions. Three-dimensional models of the same size as used in laboratory tests were built and fractured under different circumferential pressures varying from 0.1 to 0.8 MPa. Two levels of axial pressure were set, i.e., 0.4 and 0.5 MPa. As shown in Fig. 25, a fixed boundary condition was adopted on the left side of the model, and the free boundary condition was adopted on the others. The loading process was consistent with that of the laboratory tests. Axisymmetric stress elements and elastic properties with an elastic modulus of 90 MPa and a Poisson's ratio of 0.25 were used, and the maximum principal stress criterion was taken as the failure criterion. Figure 26 shows the fracture shape of the cracked model when the axial pressure and the confining pressure are 0.4 and 0.5 MPa, respectively. It can be seen that the fracture shape obtained by using the XFEM is consistent with the results of laboratory tests (Fig. 16). Figure 27 shows a comparison of the fracture dip between the numerical simulations and the tests under different loading conditions. The variation in fracture dip with loading conditions obtained by using the numerical method is in agreement with the test results, which verifies the feasibility of the simulation of the fracturing process by using the XFEM.

6 Conclusions

In this study, a hydraulic fracturing apparatus was developed to test the slurry-induced fracturing of cohesive soil. The characteristics of fracturing pressure and fracture dip were investigated. The effects of different sample parameters and loading conditions, including types of holes, unconfined compressive strength, slurry viscosity, and axial and circumferential loads, on fracturing pressure and fracture dip were examined. The conclusions are

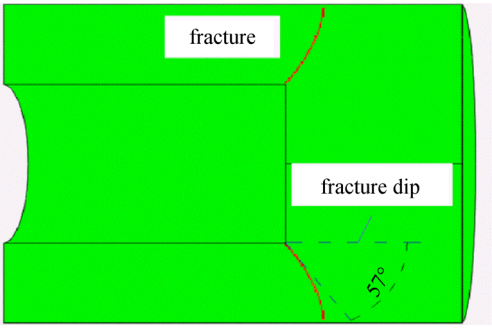

Fig. 26 Fracture shape of the cracked model (σ_c = 0.5 MPa and σ_a = 0.4 MPa).

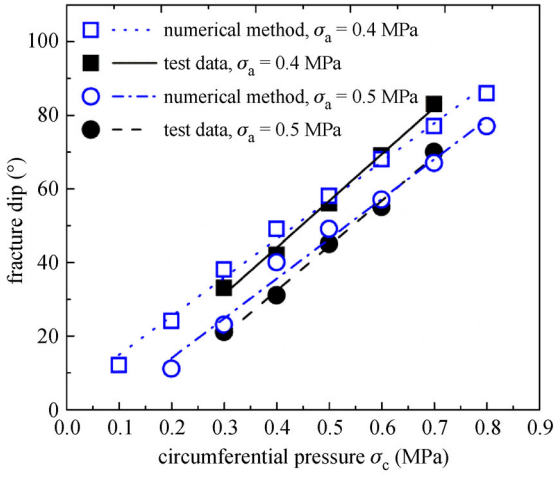

Fig. 27 Comparison of the test results and prediction of fracturing pressure.

summarized as follows.

1) The sudden decrease in slurry pressure could be the main signal for the fracturing failure of the soil. The fracture of samples with a blind hole extends obliquely from the bottom of the center hole, while the fracture of samples with a through hole follows the generatrix of the soil sample.

2) The slurry-induced fracture of the samples with a blind hole tends to extend toward the direction of the maximum principal stress. The fracture dip depends greatly on the deviator stress, and it decreases linearly with an increase in deviator stress.

3) The fracturing pressure increases linearly with the increase in the circumferential pressure, indicating that a higher overburden of the tunnel can help resist the initial fracturing induced by shield tunneling. However, the fracturing pressure was almost independent of the axial pressure. The fracturing pressure of samples with a blind hole was greater than that of those with a through hole.

4) The fracturing pressure of the soil increases with an increase in the unconfined compressive strength, and the curve follows a linear relationship. The use of a high-viscosity slurry can also increase the soil resistance to fracturing failure. However, when the slurry viscosity was >27 s, the fracturing pressure almost stabilized at 1.3 MPa and barely increased any further. The fracture dip was slightly affected by the slurry viscosity.

5) Based on the regression analysis of the test results, an empirical approach was proposed for estimating the slurry-induced fracturing of soil. The prediction results matched well with the test data, presenting an acceptable error of 5%.

Furthermore, the fracturing pressure is also related to many other factors, such as the loading speed and soil permeability, which are difficult to evaluate in tests. Phase field models [24–27] and deep neural networks [39], which aim to solve mechanical problems using computer methods, are also effective research methods for explaining phenomena that are difficult to detect experimentally. Further exploration of the influencing factors of fracturing pressure using phase field models and deep neural networks will be performed in future studies. As an exploration, this study can provide references for preventing hydraulic fracturing during slurry shield tunneling.

Acknowledgements This research was supported by the National Natural Science Foundation of China (Grant Nos. KCA313017533 and C16A300190).

References

1. Ryu Y M, Kwon Y S, Kim T H, Lee I M. Slurry clogging criteria for slurry shield tunnelling in highly permeable ground. KSCE Journal of Civil Engineering, 2019, 23(6): 2784–2793
2. Yuan D J, Huang Q F, Koizumi A, Wang M S. Study on slurry-water gushing during underwater shield tunnel construction. Journal of Rock Mechanics and Geotechnical Engineering, 2007, 026(011): 2296–2301
3. Liu X Y, Yuan D J. An *in-situ* slurry fracturing test for slurry shield tunnelling. Journal of Zhejiang University. Science A, 2014, 15(7): 465–481
4. Liu X Y, Yuan D J. Mechanical analysis of anti-buoyancy safety for a shield tunnel under water in sands. Tunnelling and Underground Space Technology, 2015, 47(3): 153–161
5. Baumert M E, Allouche E N, Moore I D. Experimental investigation of pull loads and borehole pressures during horizontal directional drilling installations. Canadian Geotechnical Journal, 2004, 41(4): 672–685
6. Nordgren R P. Propagation of a vertical hydraulic fracture. Society of Petroleum Engineers Journal, 1972, 12(04): 306–314
7. Jukkrawut T, Pornkasem J, Preecha S, Kongkitkul W, Nanakorn P. Analysis of fracture propagation in a rock mass surrounding a tunnel under high internal pressure by the element-free Galerkin method. Computers and Geotechnics, 2014, 55(1): 78–90
8. Lockner D, Byerlee J D. Hydrofracture in Weber sandstone at high confining pressure and differential stress. Journal of Geophysical Research, 1977, 82(14): 2018–2026

9. Zoback M D, Rummel F, Jung R, Raleigh C B. Laboratory hydraulic fracturing experiments in intact and pre-fractured rock. International Journal of Rock Mechanics and Mining Sciences & Geomechanics Abstracts, 1977, 14(2): 49–58
10. Ishijima Y, Kinoshita S, Ito Y, Machida K. Experimental study on hydrofracturing stress measurements. Journal of the Mining and Metallurgical Institute of Japan, 1980, 96(1114): 871–877
11. Harada T, Idemitsu T, Watanabe A. Demolition of concrete with expansive demolition agent. Doboku Gakkai Ronbunshu, 1985, 3(360): 61–70
12. Morgenstern N R, Vaughan P R. Some observations on allowable grouting pressure. In: Institution of Civil Engineers (Great Britain), International Society of Soil Mechanics and Foundation Engineering, Grouts and Drilling Muds in Engineering Practice. London: Butterworths, 1963: 36–42
13. Karol R H. Chemical Grouting and Soil Stabilization. New York: Marcel Dekker, 2003
14. Chen T L, Zhang L Y, Zhang D L. An FEM/VOF hybrid formulation for fracture grouting modelling. Computers and Geotechnics, 2014, 58(5): 14–27
15. Xiao F, Shang J, Zhao Z. DDA based grouting prediction and linkage between fracture aperture distribution and grouting characteristics. Computers and Geotechnics, 2019, 112(8): 350–369
16. Bjerrum L, Nash J K T L, Kennard R M, Gibson R E. Hydraulic fracturing in field permeability testing. Geotechnique, 1972, 22(2): 319–332
17. Qiao J L, Fan Y L, Liu B, Zhang Y P, Li Y Y. The research of backfill grouting pressure in shield tunnelling. Advanced Materials Research, 2012, 446–449: 2240–2245
18. Haimson B C. Hydraulic fracturing and rock characterization. International Journal of Rock Mechanics and Mining Sciences, 2004, 41(suppl 1): 188–194
19. Gale J F W, Gomez L A. Late opening-mode fractures in karst-brecciated dolostones of the lower Ordovician Ellenburger group, West Texas: Recognition, characterization, and implications for fluid flow. AAPG Bulletin, 2007, 91(7): 1005–1023
20. Vaughan P R. The Use of Hydraulic Fracturing Tests to Detect Crack Formation in Embankment Dam Cores. Initial Report. London: Department of Civil Engineering, Imperial College, 1971
21. Jaworski G W, Duncan J M, Seed H B. Laboratory study of hydraulic fracturing. Proceedings ASCE, 1981, 107(GT6): 713–732
22. Mori A, Tamura M. Hydrofracturing pressure of cohesive soils. Soil and Foundation, 1987, 27(1): 14–22
23. Mori A, Tamura M, Fukui Y. Fracturing pressure of soil ground by viscous materials. Soil and Foundation, 1990, 30(3): 129–136
24. Zhuang X, Zhou S, Sheng M, Li G. On the hydraulic fracturing in naturally-layered porous media using the phase field method. Engineering Geology, 2020, 266: 105306
25. Zhou S, Rabczuk T, Zhuang X. Phase field modeling of quasi-static and dynamic crack propagation: COMSOL implementation and case studies. Advances in Engineering Software, 2018, 122: 31–49
26. Zhou S, Zhuang X, Rabczuk T. Phase-field modeling of fluid-driven dynamic cracking in porous media. Computer Methods in Applied Mechanics and Engineering, 2019, 350: 169–198
27. Zhou S, Zhuang X, Rabczuk T. A phase-field modeling approach of fracture propagation in poroelastic media. Engineering Geology, 2018, 240: 189–203
28. Rabczuk T, Belytschko T. Cracking particles: A simplified meshfree method for arbitrary evolving cracks. International Journal for Numerical Methods in Engineering, 2004, 61(13): 2316–2343
29. Ren H, Zhuang X, Rabczuk T. Dual-horizon peridynamics: A stable solution to varying horizons. Computer Methods in Applied Mechanics and Engineering, 2017, 318: 762–782
30. Talebi H, Silani M, Bordas S P A, Kerfriden P, Rabczuk T. A computational library for multiscale modeling of material failure. Computational Mechanics, 2014, 53(5): 1047–1071
31. Ishida T, Chen Q, Mizuta Y, Roegiers J C. Influence of fluid viscosity on the hydraulic fracturing mechanism. Journal of Energy Resources Technology, 2004, 126(3): 190–200
32. Tiegang F, Guangqing Z. Influence of injection rate and fracturing fluid viscosity on hydraulic fracture geometry in coal. Journal of China University of Petroleum, 2014, 38(4): 117–123 (in Chinese)
33. Li X, Zhang K, Bu X, Xu W, Li N, Wei L. Evaluations of repeated fracturings in old wells. Oil Geophysical Prospecting, 2018, 53(s2): 162–167 (in Chinese)
34. Zeng L P, Qi J F, Wang Y X. Origin type of tectonic fractures and geological conditions in low-permeability reservoirs. Acta Petrolei Sinica, 2007, 28(4): 52–56 (in Chinese)
35. Xu Z H, Zhang G D, Sun D W, Sun Q C. Discussion of deviatoric stress calculation in triaxial consolidation drained test. Journal of Yangtze River Scientific Research Institute, 2016, 33(4): 57–60
36. Vu-Bac N, Lahmer T, Zhuang X, Nguyen-Thoi T, Rabczuk T. A software framework for probabilistic sensitivity analysis for computationally expensive models. Advances in Engineering Software, 2016, 100(Oct): 19–31
37. Coleman H W, Steck W G Jr, Hurlbut F C. Experimentation and uncertainty analysis for engineers. Journal of Engineering for Industry, 1991, 113(2): 248–344
38. Jin D, Shen Z, Yuan D. Effect of spatial variability on disc cutters failure during TBM tunneling in hard rock. Rock Mechanics and Rock Engineering, 2020, 53(10): 4609–4621
39. Samaniego E, Anitescu C, Goswami S, Nguyen-Thanh V M, Guo H, Hamdia K, Zhuang X, Rabczuk T. An energy approach to the solution of partial differential equations in computational mechanics via machine learning: Concepts, implementation and applications. Computer Methods in Applied Mechanics and Engineering, 2020, 362: 112790